Monolithic FFF-Printed, Biocompatible, Biodegradable, Dielectric-Conductive Microsystems

Zhumei Sun and Luis Fernando Velásquez-García, *Senior Member, IEEE*

***Abstract*— We report additively manufactured biodegradable microsystems composed of dielectric and electrically conductive layers. The devices were made via fused filament fabrication (FFF), which is arguably the simplest and cheapest commercial 3-D printing technology, done with the most inexpensive printing hardware. The base constitutive material is polylactic acid (PLA)–a biodegradable polymer made of cornstarch that can be doped with micro and nanoparticles to change its physical properties, e.g., become electrically conductive. The devices were monolithically manufactured using a commercial dual extruder 3-D-printer. The feature resolution and surface topography of the printing technology was characterized for both dielectric and conductive materials; their outgassing rates were measured and their cytotoxicity was investigated. The gauge factor of the conductive PLA was measured. Basic electrical components, cantilevers, and electrohydrodynamic liquid ionizers with integrated extractor electrode and threaded microfluidic port were demonstrated. [2017-0118]**

***Index Terms*— Additively manufactured microelectromechanical systems (MEMS), biocompatible MEMS, biodegradable MEMS, cantilever, electrospray, microfluidics, multi-material 3-D printed microsystems.**

I. Introduction

MICROELECTROMECHANICAL systems (MEMS) harness miniaturization to improve device and system performance; over the course of several decades, a wide variety of MEMS have been demonstrated including sensors, actuators, frequency sources, and microfluidics [1]. However, only a handful of these microsystems have become commercial products, e.g., inertial sensors and pressure sensors, which are either devices that are produced in great quantities at a low per-unit cost, or are part of high-end products [2]. The large cost associated with making microfabricated devices is related to the use of semiconductor cleanrooms, which are specialized manufacturing environments that are very expensive to build and run, operated by users that are highly trained. This is justified in cases where the microsystem has very small features or requires extreme control of the impurities; however, there are quite a few examples of microsystems that don't necessitate these specifications. Furthermore, in many cases their designs are constrained by the requirements of the cleanroom such as the small pool of compatible materials, the planarity of the substrates that can be processed, and the geometry of features that can be created. Therefore, manufacturing technologies that reduce the time and cost spent per design loop, that widen the choice of materials, and that can accommodate freeform feature morphology while reliably generating feature sizes of interest could decisively contribute to the commercialization of MEMS that don't have to be made in a semiconductor cleanroom.

Additive manufacturing (AM), i.e., the layer-by-layer construction of devices using a computer-aided design (CAD) file [3], has recently been explored as a manufacturing toolbox for MEMS; researchers have shown 3-D printed MEMS with performance on par or better than counterparts made with standard microfabrication [4]–[7]. In addition, via 3-D printing designs not previously attainable due to fabrication complexity or system three-dimensionality have been demonstrated, e.g., multiplexed electrohydrodynamic compound droplet generators [8] and free-standing helical electrical probes [9]. However, all these examples are one-material devices, that is, they are made of a single substance that is shaped to accomplish a certain task, e.g., distribute liquid, restrict fluid flow, or transport electrical current.

A very promising research opportunity in 3-D printed MEMS is the demonstration of monolithic multi-material devices, i.e., where different parts of the microsystem are made of different materials, and where the system does not require significant post-assembly/post-processing [10]. The simplest multi-material manufacturing platform has two constitutive materials; using a support material to create cavities inside a constitutive material, as in polyjet printing [11], does not fall into the two-material category because the support material circumvents limitations of the printing method instead of providing more capabilities to the microsystem. Recently, the group of L. Lin at UC Berkeley reported 3-D printed dielectric-conductive miniaturized components [12]. Strictly speaking, the conductive material in these devices, i.e., silver paste, is not printed but micromolded by feeding it into the cavities of polyjet-printed structures via a syringe after removing the support material. It would be advantageous to print structures composed of dielectric and conductive layers without the limitations caused by micromolding the conductive material, e.g., mass transport and structural integrity issues when removing the support material, bubble trapping and wettability/surface interaction issues when filling-in cavities with conductive material. In addition, it would be advantageous to monolithically print all the materials using the same printing technology to minimize issues of post-processing and/or post-assembly.

Manuscript received May 25, 2017; revised July 31, 2017; accepted August 25, 2017. Date of publication October 4, 2017; date of current version November 29, 2017. Subject Editor S. M. Spearing. *(Corresponding author: Luis Fernando Velásquez-García.)*

Z. Sun is with the Mechanical Engineering Department, Massachusetts Institute of Technology, Cambridge, MA 02139 USA (e-mail: zhumeis@mit.edu).

L. F. Velásquez-García is with the Microsystems Technology Laboratories, Massachusetts Institute of Technology, Cambridge, MA 02139 USA (e-mail: velasquez@alum.mit.edu).

Color versions of one or more of the figures in this paper are available online at http://ieeexplore.ieee.org.

Digital Object Identifier 10.1109/JMEMS.2017.2746627

Fused filament fabrication (FFF) is an AM technique based on extrusion of thermoplastic polymers [13]; FFF is arguably the simplest and cheapest commercial 3-D printing technology available, conducted with the most inexpensive printing hardware (as a comparison, a reliable single-nozzle FFF printer with heated bed currently costs as little as $220 [14], while an equivalent stereolithography (SLA) printer costs $3,500 [15]). There has been little reported work on FFF-printed MEMS, in favor of other AM techniques such as SLA, polyjet, and inkjet printing [16]. However, FFF offers a number of attractive features for making 3-D printed miniaturized systems:

1) FFF printers can process most thermoplastics, covering a wide range of chemical resistance, flexibility, maximum elongation, and stress yield. FFF printers can typically heat up the feedstock up to 250 °C, which is adequate to print polylactic acid (PLA), acrylonitrile butadiene styrene (ABS), nylon, polyethylene terephthalate (PET), and thermoplastic elastomer (TPE). Some printers can go even higher and process plastics such as polycarbonate (PC) and polyether ether ketone (PEEK) [17].
2) There is commercially available doped thermoplastic feedstock (thermoplastic mixed with micro/nanoparticles) with physical properties greatly different from those of the undoped material. For example, the doped feedstock can be electrically conductive, ferromagnetic, phosphorescent, thermochromic, or photochromic. These materials could be used to create a wide range of low-cost sensors and actuators.
3) There are commercial FFF printers that can deposit a plurality of materials using independent nozzles, making possible the monolithic fabrication of multi-material microsystems in a single print run; printers with up to 5 independent nozzles are commercially available [18]. In contrast, SLA printers process only one material per print run; also, polyjet printers can monolithically print multi-material objects, but the available printable feedstock only covers changes in color, transparency, stiffness, and deformability, or are support materials [19].
4) In general, FFF-printed objects don't require significant post-processing. In particular, watertight closed channels can be printed without involving a support material (i.e., the nozzle can extrude material on top of the gap between two adjacent walls to create the ceiling of a channel).
5) FFF printable feedstock is cheaper than that of competing AM technologies. As a comparison, in August of 2017 1L of SLA resin costs ∼$350, a 3L container of polyjet resin costs ∼$500 - $1,250, and a 1Kg spool of FFF filament costs ∼$30-$100. Therefore, the printable material needed to make a 1-cm^3 device costs on the order of several dollars if printed with SLA or polyjet and tens of cents if printed with FFF.

This article reports FFF-printed, biodegradable, dielectric-conductive microsystems. The base constitutive material is PLA –a compostable thermoplastic made from renewable sources (e.g., cornstarch) [20] with biocompatibility that greatly exceeds that of most printable materials [21]. Even though PLA is biodegradable, it is resistant to a wide variety of solvents, e.g., ether, hexane, propanol, and ethanol [22]. PLA is an excellent electrical insulator, but it can be doped with micro/nanoparticles to become electrically conductive. Section II describes the fabrication of the devices using a commercial dual extruder 3D-printer. Section III reports the characterization of the resolution and surface topography of the PLA FFF-printed objects, while Section IV describes their vacuum outgassing characterization. Section V addresses the biocompatibility of FFF-printed PLA feedstock, while section VI reports the piezoresistivity characterization of FFF-printed graphite-doped PLA. Section VII provides selected proof-of-concept examples of biodegradable microsystems monolithically made of dielectric and conductive layers: basic electrical components, cantilevers, and electrohydrodynamic liquid ionizers. Finally, Section VIII summarizes the work and suggests directions for future research.

II. Fabrication

The devices were made with a dual extruder 3-D printer MAKEiT PRO-M (MAKEiT, Inc., Alhambra, CA). The printer uses 1.75 mm diameter filament feedstock, has a 7.9-inch cube building volume, can heat up the feedstock up to 275 °C, and has a heated bed with detachable build plate that can heat up to 120 °C. The printer can use nozzles with diameters between 0.2 mm and 1.0 mm, but the work reported in this article was done with 0.4 mm nozzles (in our experience, nozzles with smaller diameter easily get clogged when processing doped thermoplastics). The printer is kept inside a Model 600 enclosure (3DPrintClean, Mountainside, NJ) that recirculates air while removing volatile organic compounds (VOCs) and particles using high-efficiency particulate air (HEPA) filtering [23].

Clear PLA filament from 3D-Fuel (3DomFuel, LLC, Fargo, ND) was used as the dielectric feedstock; although PLA is sold in a great variety of colors, clear PLA was chosen to help visualize the dielectric layers and/or facilitate the use of the printed devices in microfluidic applications; in addition, pure PLA is transparent. Four different electrically conductive PLA filaments were preliminarily screened for this study: the graphite-doped "proto-pasta" (ProtoPlant, Vancouver, WA), the metal nanoparticle-doped "electrify" (Multi3D, Cary, NC), the graphene-doped "F-electric" (Functionalize, Inc., Seattle, WA) and a second graphene-doped filament from a different vendor (Black Magic 3D, Calverton, NY). Even though the electrical resistivity of the graphene-doped filaments is ∼1 Ω·cm and that of the metal nanoparticle-doped filament is ∼5 mΩ.cm, the ∼10 Ω · cm proto-pasta filament was selected for this study because it was the only filament we tried that worked reliably with our printer. There are two possible explanations for the lack of reliability when printing with the other conductive filaments. First, like most FFF printers, the MAKEiT is of the bowden type, i.e., the stepper motor that feeds the filament to the nozzle is not right next to the extruder but connected through a flexible tube, which can cause problems when trying to feed filaments that are not stiff enough –this was clearly the limitation of the metal nanoparticle-doped

filament. Second, the graphene-doped filaments degrade while heating up the material, so the printing job needs to occur right after the filament is fed to the nozzle; in our experiments we found that the graphene filaments could clog the nozzle while waiting for the other nozzle to finish printing a dielectric layer.

To print a device, a CAD model is created in *stl* format and exported to a slicer software, which is a script that discretizes the 3-D model into a set of horizontal cuts, i.e., *slices*, and creates a *gcode* file with the traveling path to raster each slice with associated conditions for each nozzle (e.g., nozzle temperature, bed temperature, feedstock feed rate, nozzle speed, cooling fan speed). The slicer software Simplify3D was used in this work because it allows very fine control of the gcode file and it also creates reliable files for dual nozzle printing. The gcode file is then transferred to the 3-D printer using a flash memory card. The printed object is composed of two different kinds of structures: (i) the *shell*, which is made of one or more closed loops per slice that follow the surfaces of the object, and (ii) the *infill*, which is a cellular structure (e.g., a honeycomb) with walls made of overlapping strokes that provides mechanical support to the shell. For printing two-material devices, decoy structures were included to ensure that the feedstock was flowing properly from the nozzle intended to be active (in general, FFF printers don't sense whether the nozzle is ejecting feedstock). To print dielectric PLA, the temperature of the bed and the nozzle were set at 65 °C and 200 °C, respectively; to print conductive PLA, the temperature of the bed and the nozzle were set at 50 °C and 225 °C, respectively. We found excellent adhesion between dielectric and conductive PLA layers (e.g., a monolithically printed structure composed of a 2-cm wide cube made of conductive PLA, stacked between two 2-cm wide cubes made of dielectric PLA, did not detach at the interface between dielectric PLA and conductive PLA layers when pulled hard by hand). After printing, the parts were removed after the bed temperature fell below 40 °C.

Removing FFF-printed miniaturized devices from the build platform posed challenges. The standard approach is to use a spatula, which is not ideal because it can scratch the build plate, which could affect the quality of the bottom surface in future prints. Grabbing the printed object with pliers can work if the device is tall and thick enough, but this procedure can also scratch the surfaces that interact with the tool. Instead, we included in the layout of the printed parts an M6 threaded hole with 1-mm thread pitch that was used to insert a screw to cleanly remove the parts. The printed microfluidic devices had M6 fluidic ports that were used for dismounting the parts, while the metrology samples and electrical components included a 3-mm thick base plate with a M6 threaded hole monolithically printed with the rest of the structure. The outgassing samples and the samples used to characterize the piezoresistivity of the graphite-doped PLA were large enough to be removed by slightly bending the build plate. The 2-cm wide cubes used to characterize the surface topography, as well as the 6 mm by 6mm by 2 mm tiles used in the cytotoxicity study, were removed by hand using nitrile rubber gloves while carefully exerting an in-plane twisting movement (in the case of the samples for the cytotoxicity study, each tile was printed with a 6 mm by 2 mm side touching the build plate to facilitate its removal).

III. Voxel and Surface Topography Characterization

A key aspect for 3-D printing detail-rich objects is how small and repeatable are the voxels. In SLA or polyjet printing the printers have pixels, whose size is a measure of the resolution and repeatability of the voxels in the XY plane. In FFF, the height of the voxels is defined by the nozzle diameter and the stepping of a motor that controls the out-of-plane movement, while the width of the voxels is defined by the nozzle diameter and the motors that control the in-plane movement. In our experience, the height of the trace printed by a nozzle can be varied roughly between 25% and 75% the nozzle diameter; shorter layers can clog the nozzle, and taller layers are not reliably controlled. The width of the trace printed by the nozzle is on the order of the nozzle diameter; although the slicer software employed in this study creates the slices using closed-loop traces, the minimum wall thickness that can be created is still on the order of one nozzle diameter because the slicer software allows significant overlapping between adjacent traces. In addition, it is possible to reliably define gaps that are smaller than the nozzle diameter. In this work, down to 500 μm-thick walls were consistently defined, and gaps as small as 200 μm were consistently resolved.

Test structures were printed and measured to characterize the surface topography, as well as the in-plane (XY) and out-of-plane (Z) feature size and resolution. Metrology of the solid XY and Z features was conducted with a 0-1" digital electronic micrometer (iGaging, San Clemente, CA) with 1 μm resolution and 3 μm accuracy. The structures used to characterize the void XY features were measured with a Mighty Scope® digital microscope (Aven, Ann Arbor, MI) with 5 megapixel CMOS camera, 10X to 200X magnification, and 5 μm precision, while the surface topography was characterized with a Bruker DektakXT stylus profiler with 2 μm radius tip applying a 2 mg load; the topography of the samples was analyzed using the standards ISO 4287 [24] and 4288 [25]. The XY and Z metrology reported in this section came from measuring structures made in dielectric PLA; however, analogous metrology conducted on conductive PLA samples yielded similar results. Therefore, the voxel resolution and repeatability seems to be controlled to first order by the positioning precision of the XYZ movement of the printer. Also, the data suggest that the final dimensions of the printed parts were not visibly affected by the differences in rheology of the printable feedstock and/or the differences in rheology were small (the conductive PLA might be more viscous at a given extrusion temperature given the presence of the dopant, but the material was deposited hotter than the undoped PLA feedstock). Nonetheless, differences in the surface topography between conductive PLA and dielectric PLA samples were identified.

A. Layer height characterization

Stair-like structures (Fig. 1) were printed and measured to characterize the height of the printed traces; the data are shown

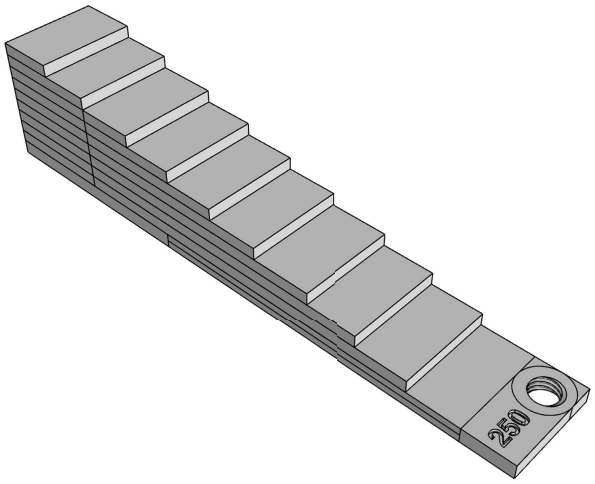

Fig. 1. Schematic (not drawn to scale) of the test structure used to characterize the printing precision and repeatability of the out-of-plane features. The structure is a nine-step stairs on top of a base with a threaded hole. The height of the steps is the nominal slicing height, varied between 100 μm and 250 μm.

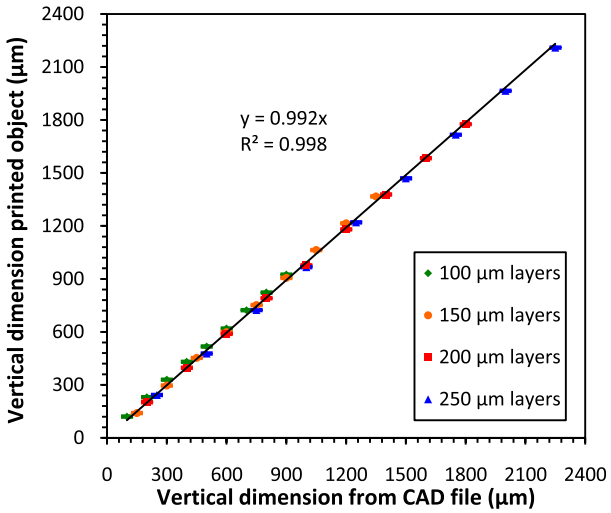

Fig. 2. Height of the printed steps (dielectric PLA) vs. corresponding CAD dimensions. Each data point is the average of 100 measurements. The standard deviation across all data sets is 5 μm.

in Fig. 2. The structure had a total of 9 steps on top of a 3 mm-thick base plate with an M6 threaded hole. The height of the steps is the nominal slicing height, which was set at 100 μm, 150 μm, 200 μm, and 250 μm. For each of the four slicing heights, 25 structures were printed and measured in four points within each step (i.e., each data point in Fig. 2 is the average of 100 measurements). In all cases, we found that the height of the base of the printed stair structure was equal to 3.25 mm instead of 3 mm; the extra thickness was probably due to the specifications to print the first layer, which is critical to ensure adhesion of the part to the build plate. The 0.25 mm extra height is not set (or can be varied) by the slicing software, but by the firmware of the printer. The average heights of the printed layers closely match those of the CAD files, i.e., are about 0.8% off from the 1-to-1 ideal correspondence. The standard deviation across all data sets is 5 μm, comparable

TABLE I

AVERAGE IN-PLANE DIMENSION AND STANDARD DEVIATION FOR PRINTED 2-cm WIDE CUBES (DIELECTRIC PLA) USING DIFFERENT SLICING HEIGHTS

Slice height (µm)	Average (mm), N = 25	Standard deviation (µm)
100	19.871 (X) 19.861 (Y)	22 (X) 20 (Y)
150	19.831 (X) 19.840 (Y)	17 (X) 18 (Y)
200	19.859 (X) 19.851 (Y)	25 (X) 22 (Y)
250	19.880 (X) 19.885 (Y)	22 (X) 22 (Y)

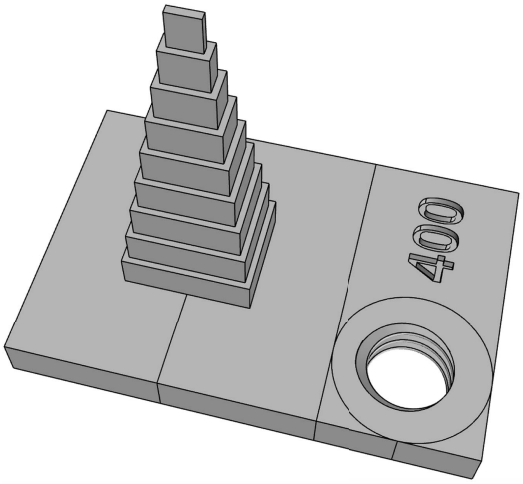

Fig. 3. Schematic (not drawn to scale) of the test structure used to characterize the printing precision and repeatability of the in-plane solid features. The structure is a pyramid composed of nine 2.4 mm-tall steps on top of a 3-mm thick base with an M6 threaded hole. The width of the steps was varied between 100 μm and 400 μm.

to the repeatability of the metrology instrument, and does not seem to be a function of the slicing height.

B. In-plane solid feature characterization

First, the in-plane dimensions of 2-cm wide (from the CAD file) printed cubes were measured to assess any differences between nominally identical objects printed with different slicing height. For each slicing height (100 μm, 150 μm, 200 μm, and 250 μm), 25 cubes were printed and measured; the results are shown in Table I. No noticeable difference was obtained in the average dimension and standard deviation between the X and Y directions (the X direction corresponds to the narrower dimension of the build plate), and the average values and standard deviations were very close for all slicing heights. Therefore, it was concluded that the metrology of prints made with one slice height is representative of the resolution and repeatability of in-plane solid features achieved using other slice heights.

Step pyramids (Fig. 3) were printed using 150 μm layers and measured in both X and Y directions to characterize the in-plane solid feature resolution and repeatability. Each pyramid had nine 2.4 mm-tall steps on top of a 3 mm-thick plate with an M6 threaded hole. The steps were concentric and the separation between the edges of adjacent steps was

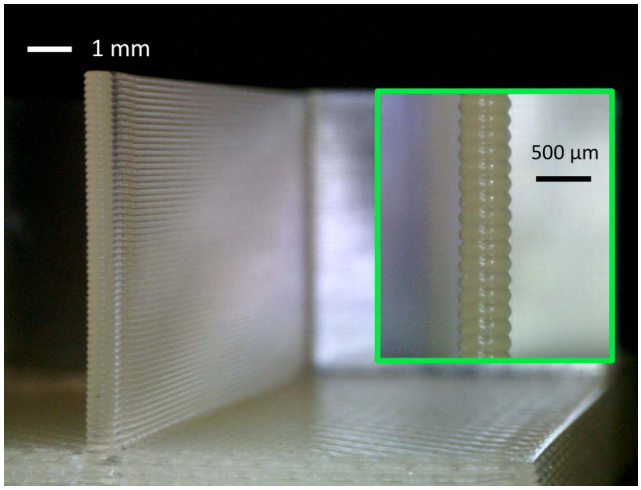

Fig. 4. A 0.5 mm thick wall made of dielectric PLA with close-up of the vertical scalloping.

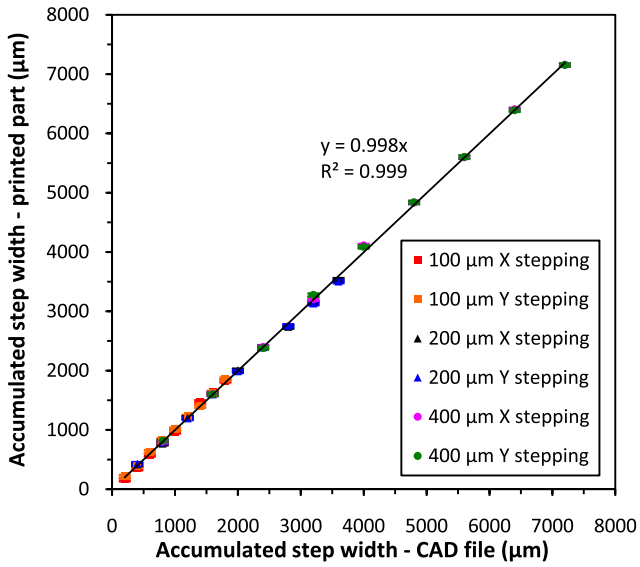

Fig. 5. Accumulated step width of the printed part (dielectric PLA) over the dimensions of the smallest step vs. corresponding CAD dimension for sets of step pyramids with separation between edges for adjacent steps equal to 100 μm, 200 μm, and 400 μm. Each data point is the average of 30 measurements. The standard deviation across all data sets is 25 μm.

set to 100 μm, 200 μm, and 400 μm. By trial and error it was determined that the larger in-plane dimension of the step had to be at least 2 mm (about 5 nozzle diameters) for the printer to resolve the step well; in the narrower dimension of the step, the smallest feature that we could print was 0.5 mm (Fig. 4); therefore, in all cases the smallest step of the pyramid was at its top and measured 2 mm by 0.5 mm. A total of 30 pyramids for each separation between the edges of adjacent steps were printed and measured; the results are shown in Fig. 5. The average measured dimension is off about 0.15% compared to the corresponding dimension from the CAD file. Also, no significant differences were found in the average and standard deviation between the X and Y measurements. In addition, we saw no difference in the metrology when the narrower side of the step lined up with

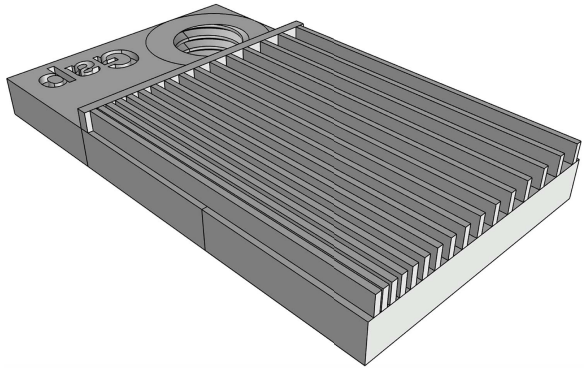

Fig. 6. Schematic (not drawn to scale) of the test structure used to characterize the printing precision and repeatability of the in-plane void features. The structure is a comb with 600 μm-tall, 500 μm-wide, and 25 mm-long fingers on top of a base with a threaded hole. The gap between adjacent fingers was varied between 100 μm and 1500 μm in steps of 100 μm.

the X-axis or the Y-axis. The standard deviation across all data sets is 25 μm, i.e., about 5 times the standard deviation in Z, which is probably explained by the use of a less precise mechanism to move the printing head relative to the bed in the X and Y directions (the Z movement is made entirely of computer numerical control (CNC) machined parts, while the X and Y movements include rubber transmission bands). The minimum dimensions of the solid XY features are significantly larger than those typically obtained in high-resolution digital light projection (DLP)/SLA printing ($\sim$75 μm [26]). However, dimensions above the minimum feature size can be finely adjusted and the variation in the XY dimensions compares well with the typical variation found in SLA and polyjet printers, which is on the order of 1 pixel (typical pixel size of a DLP/SLA printer is 25-50 μm and typical pixel size of a polyjet printer is 42 μm).

C. In-plane void feature characterization

The test structures for the characterization of the resolution and repeatability of the in-plane void features are combs with varying finger separation (Fig. 6); the combs are on top of a 3-mm thick plate with an M6 threaded hole. A set of 25 identical structures were printed using 150 μm layers; the combs were 600 μm tall with fingers 25 mm long and 500 μm wide, while the separation between adjacent fingers was varied between 1500 μm and 100 μm in steps of 100 μm. For each test structure, the gaps between the comb fingers were measured in 4 points across the length of the fingers; the results of the metrology are shown in Fig. 7. There is a linear dependence between the average measured gap and the corresponding feature from the CAD file, and there is clearly an offset of about 70 μm that makes the printed gaps consistently smaller than the gaps in the CAD file; however, gaps smaller than 200 μm could not be reliably printed. Perhaps the creation of narrower gaps comes from reflow of the printed material right in front of the hot nozzle while depositing the trace that defines the gap. The standard deviation across all data sets is 28 μm, which is similar to the

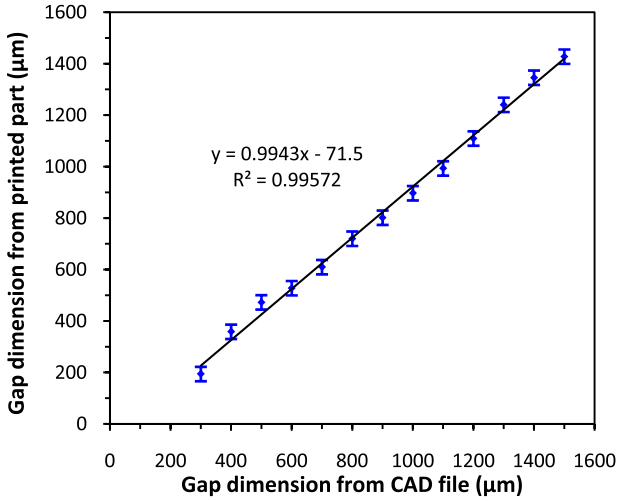

Fig. 7. Measured gap in printed parts (dielectric PLA) vs. corresponding CAD dimensions. Each data point is the average of 100 measurements. The standard deviation across all data sets is 28 μm.

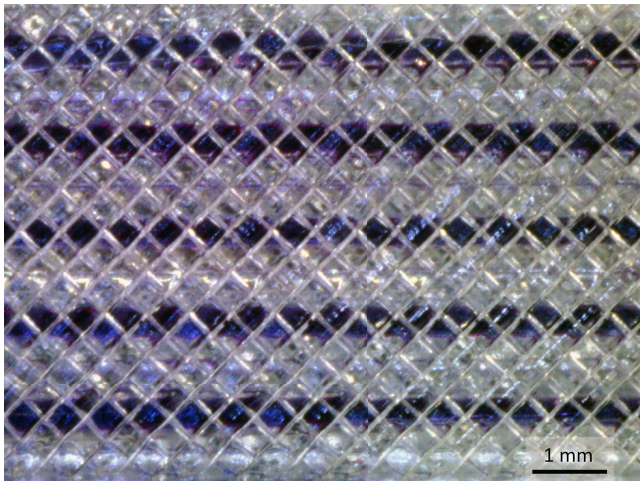

Fig. 8. Microchannels with 300 μm $\times$ 300 μm cross-section printed in clear PLA using 150 μm layers; the top of the channels is 600 μm thick.

standard deviation obtained in the metrology of the in-plane solid features.

FFF printing can create closed channels without any kind of post processing, e.g., removal of support material, simply by extruding feedstock on top of the gap between two adjacent walls –this procedure is called *bridging* by the 3-D printing community. Aspects that influence how long a gap can be bridged include the temperatures of the nozzle and the bed, the printing speed, how far is the nozzle from the heated bed, the height of the layers, and the specifications of the forced-air cooling and of the atmosphere surrounding the printer. In this study, gaps of up to ~1 mm in length were bridged. However, careful tuning of the printing profile can result in bridging significantly larger gaps [27]. The overlapping between adjacent PLA traces can be set to create leak-free prints. As an example, Fig. 8 shows a linear array of 5 watertight microchannels with 300 μm $\times$ 300 μm cross-section flowing water mixed with the tracer dye Fluorescent FWT red (Kingscote Chemicals, Miamisburg, OH).

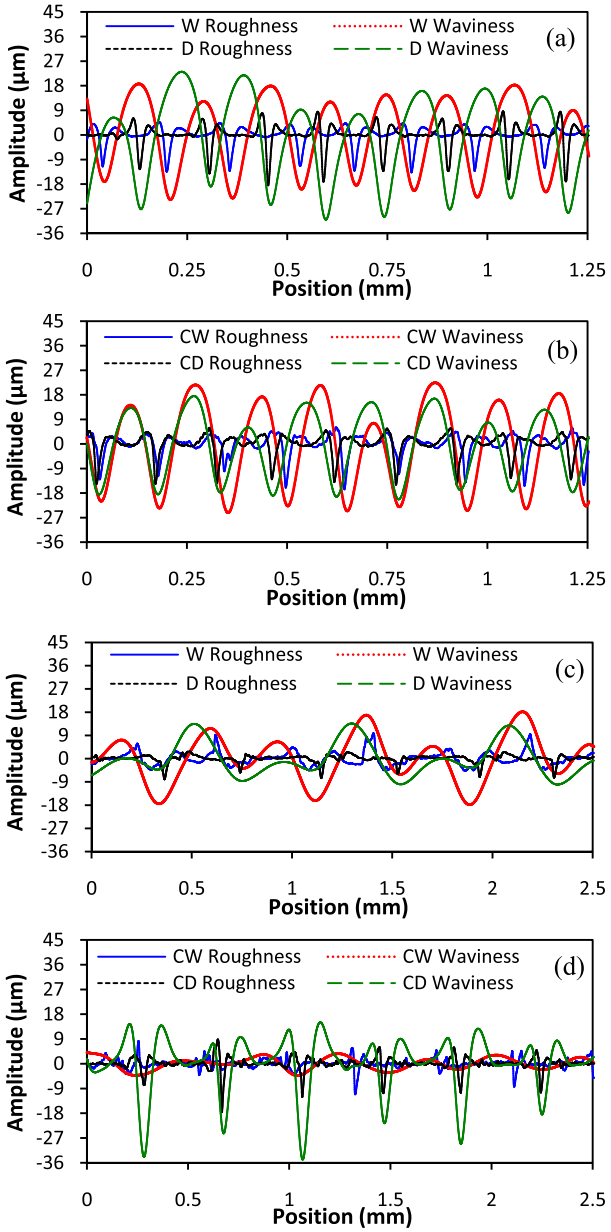

Fig. 9. (a) Vertical roughness and waviness, dielectric PLA; (b) vertical roughness and waviness, conductive PLA; (c) horizontal roughness and waviness, dielectric PLA; (d) horizontal roughness and waviness, conductive PLA. In the plots D = dielectric PLA, dense setting; W = dielectric PLA, watertight setting; CD = conductive PLA, dense setting; CW = conductive PLA, watertight setting.

D. Surface topography characterization

The surface waviness –long-range surface texture due to the printed strokes that makeup the shell of the object, and the roughness –short-range surface texture within each stroke of printed material, were characterized on both vertical and horizontal surfaces for both dielectric and conductive PLA using 2-cm wide cubes printed with 150 μm layers. In these experiments two different printing settings were used: the *dense printing setting* has 50% infill overlap (amount of overlapping between adjacent strokes), while the *watertight printing setting* has 75% infill overlap. Plots of the horizontal and vertical topography are shown in Fig. 9, while a

TABLE II

VERTICAL WAVINESS PERIOD, VERTICAL WAVINESS PEAK-TO-VALLEY HEIGHT, VERTICAL RA, AND VERTICAL RQ OF FFF-PRINTED PLA SAMPLES

Sample	Period (μm)	Peak-to-valley height (μm)	Ra (μm)	Rq (μm)
D	148.73 ±0.10	33.95±0.44	2.36±0.06	3.03±0.06
W	149.65 ±0.33	32.63±0.32	2.24±0.02	2.91±0.04
CD	148.26 ±0.66	32.11±0.23	2.54±0.05	3.31±0.07
CW	148.65±0.59	41.01±0.26	2.88±0.84	3.65±0.11

TABLE III

HORIZONTAL WAVINESS PERIOD, HORIZONTAL WAVINESS PEAK-TO-VALLEY HEIGHT, HORIZONTAL RA, AND HORIZONTAL RQ OF FFF-PRINTED PLA SAMPLES

Sample	Period (μm)	Peak-to-valley height (μm)	Ra (μm)	Rq (μm)
D	778.62±3.14	25.51±2.10	1.13±0.12	1.59±0.20
W	779.04±7.53	36.32±3.74	2.22±0.20	2.84±0.28
CD	786.51±19.30	42.57±5.15	1.36±0.18	1.71±0.21
CW	782.34±27.14	6.62±0.97	1.12±0.14	1.69±0.27

summary of the vertical surface topography metrology is shown in Table II and a summary of the horizontal surface topography metrology is shown in Table III. On the one hand, the shape of the vertical waviness for both kinds of feedstock and printing settings are very similar –roughly a sinusoidal with slightly wider peaks and narrower valleys (Fig. 9(a) and (b)). On the other hand, the shape of the horizontal waviness is different for each kind of feedstock and printing settings: in the W and D samples the shape of the horizontal waviness is composed of a peak and a valley with smaller amplitude followed by a peak and a valley with larger amplitude (Fig. 9(c)), while in the CW samples the shape looks like a sinusoidal, and in the CD samples the shape has two short peaks followed by a deep valley (Fig. 9(d)). The variation in the shape of the horizontal waviness across the samples suggests that the material flows differently for each kind of feedstock and infill setting. The periods of the vertical waviness are on average 0.8% off the nominal 150-μm slicing with <1 μm standard deviation –confirming the slope found in the out-of-plane metrology and evidencing that the majority of the standard deviation in the out-of-plane metrology was caused by the instrument. Also, the peak-to-valley height is close to $\sim$25% of the period, and the roughness is on the order of 2-4 μm. In addition, the horizontal roughness is on the order of 1-3 μm, but the peak-to-valley height greatly varies between $\sim$5% and 28% of the slicing height. In all cases, the period of the horizontal waviness is very similar and close to two nozzle diameters (800 μm), which suggests that is mostly caused by the nozzle movement.

IV. OUTGASSING CHARACTERIZATION

The outgassing in vacuum of FFF-printed dielectric and conductive PLA samples was characterized in a custom-made testing rig. The apparatus is a 200 mm-wide, ultra-high vacuum (UHV) compatible stainless steel cube chamber fitted with a 200 amu reduced gas analyzer (Hiden Analytical, Peterborough, NH) that is capable of measuring partial pressures as small as 1×10^{-14} mbar; the system is pumped by a 68 l/s dry rough pump/turbo combo capable of 10^{-10} mbar ultimate pressure (if baked). The samples had a nominal surface area equal to 100 cm^2. Measurement of the outgassing rates was conducted every ten minutes for over 10 hr; the experimental results at 1 hr and 10 hr are provided in this study. In the case of the dielectric PLA sample, the main component of the outgassing is water (Table IV); this is expected because the samples were not baked within the chamber. The partial pressure of hydrocarbons mixed in the vacuum is over two hundred times smaller than the contribution from water, evidencing that the clear PLA releases very little constitutive material; this is confirmed by the lack of spectrum peaks above 55 amu (Fig. 10). In the case of the conductive PLA, the majority of the outgassing is still water, but the outgassing due to hydrocarbons is now comparable to the outgassing from water (Table V). The conductive PLA clearly releases significantly more hydrocarbons, which is confirmed by the large amount of peaks in the spectrum and the presence of peaks as heavy as 149 amu (Fig. 11). The 1-hour outgassing rate for the two kinds of PLA is about the same, but the 10-hour outgassing rate for clear, dielectric PLA is almost six times smaller than the corresponding outgassing rate from the conductive PLA. However, both kinds of PLA are

TABLE IV

OUTGASSING RATE - DIELECTRIC PLA

1 hour	10 hour
$Q_{total} = 5.9\times10^{-7}$ mbar.l/(s.cm^2)	$Q_{total} = 1.1\times10^{-8}$ mbar.l/(s.cm^2)
$Q_{H2O} = 2.9\times10^{-7}$ mbar.l/(s.cm^2)	$Q_{H2O} = 2.7\times10^{-9}$ mbar.l/(s.cm^2)
$Q_{CxHy} = 9.1\times10^{-10}$ mbar.l/(s.cm^2)	$Q_{CxHy} = 1.3\times10^{-11}$ mbar.l/(s.cm^2)
Pressure = 8.39×10^{-7} mbar	Pressure = 1.50×10^{-8} mbar

In all cases, the outgassing of the background was subtracted.

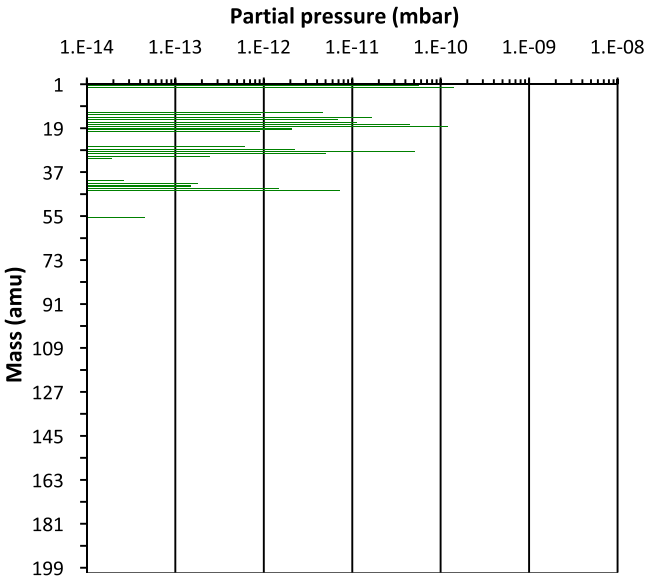

Fig. 10. Mass spectrum (dielectric PLA) after pumping down for 10 hours.

TABLE V
OUTGASSING RATE - CONDUCTIVE PLA

1 hour	10 hour
$Q_{total} = 5.1\times10^{-7}$ mbar.l/(s.cm^2)	$Q_{total} = 6.8\times10^{-8}$ mbar.l/(s.cm^2)
$Q_{H2O} = 2.1\times10^{-7}$ mbar.l/(s.cm^2)	$Q_{H2O} = 6.9\times10^{-9}$ mbar.l/(s.cm^2)
$Q_{CxHy} = 1.3\times10^{-8}$ mbar.l/(s.cm^2)	$Q_{CxHy} = 4.6\times10^{-9}$ mbar.l/(s.cm^2)
Pressure = 7.26×10^{-7} mbar	Pressure = 9.56×10^{-8} mbar

In all cases, the outgassing of the background was subtracted.

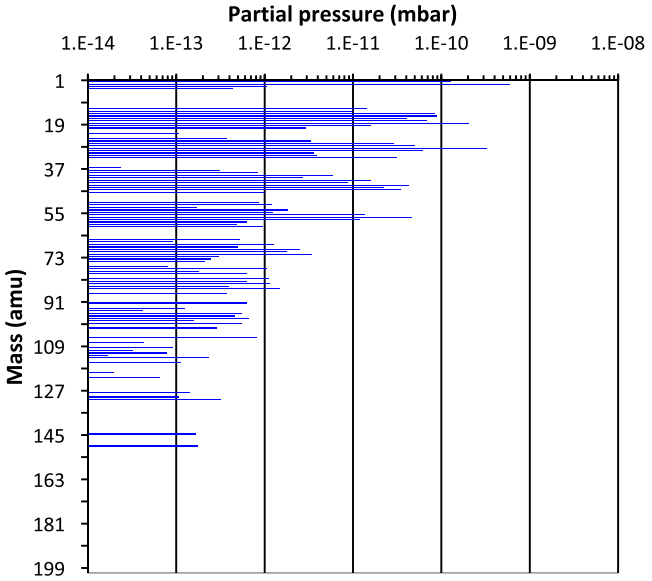

Fig. 11. Mass spectrum (conductive PLA) after pumping down for 10 hours.

high-vacuum (HV) compatible [28]. In particular, the 10-hour outgassing rate of the dielectric PLA is similar to that of unbaked, polished and degreased aluminum [29], while the 10-hour outgassing rate of the conductive PLA is smaller than the outgassing rate of nylon, PTFE, and polyethylene [30].

V. BIOCOMPATIBILITY CHARACTERIZATION

A cytotoxicity study was conducted on 6 mm by 6 mm by 2 mm FFF-printed tiles made of dielectric PLA and conductive PLA to assess the biocompatibility of the feedstock. Prior to cell exposure, the printed samples were soaked in a 70% ethanol, 5% isopropanol, and 25% distilled water solution (by volume) for 30 minutes at room temperature. Samples were then rinsed five times with distilled water, transferred to clean wells in a Falcon® 24-well plate (Corning, Inc., Corning, New York), and subjected to a final rinse in phosphate buffered saline (PBS). Jurkat immortalized human T-lymphocytes grown in Roswell Park Memorial Institute (RPMI) medium with 10% fetal bovine serum (FBS) and 1:100 penicillin/streptomycin medium, were seeded into wells containing either a dielectric PLA tile (3 samples in total, 1 per well), a graphite doped-PLA tile (3 samples in total, 1 per well), or no tile (3 wells in total) at a density of 250,000 cells/mL at a volume of 1 mL per well.

Cell viability was assessed immediately after seeding, and after 48 hours of incubation at 37 °C using the PrestoBlue®

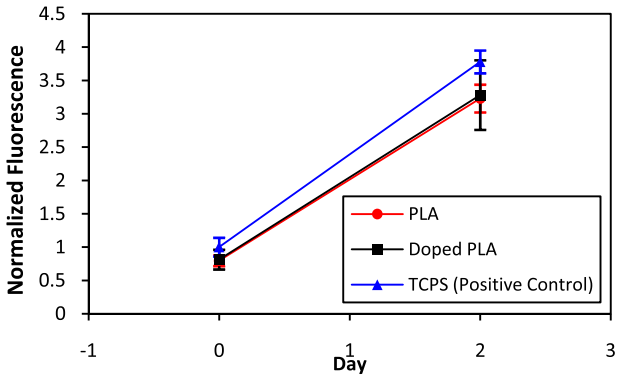

Fig. 12. Normalized fluorescence vs. time for Jurkat immortalized human T-lymphocytes in contact with dielectric PLA (PLA), conductive PLA (doped PLA) and the positive control. Each data point is the average of 3 measurements.

Cell Viability Reagent. From each sample well, 90 μL of cell solution was transferred to an opaque-bottom, 96 well-plate well along with 10 μL of PrestoBlue® Cell Viability Reagent. Additionally, wells of cell media, without cells, and reagent were incorporated into the assay to act as blanks. Wells were mixed thoroughly, and the cells and reagent incubated for one hour at a temperature of 37 °C. A SpectraMax M2 Microplate reader (Molecular Devices, Sunnyvale, CA) measured the fluorescence levels of the assay wells at an excitation of 560 nm and an emission of 590 nm. Fluorescence values for the media-only treatment group were averaged and subtracted from the fluorescence readings obtained from the remaining treatment groups (i.e., PLA, doped-PLA, and positive control of cells grown in tissue culture polystyrene (TCPS)). The blank-corrected values were then averaged across each treatment group. The reported values in Fig. 12 were normalized to the blank-corrected, TCPS average measured immediately after seeding. The viability of cells exposed to printed dielectric PLA and conductive PLA for 48 hours exhibited no statistically significant decline in cell viability relative to the positive control. Furthermore, the cells exposed to the conductive PLA exhibited a response not statistically different from to cells exposed to dielectric PLA, which is known to be biocompatible [21]. This result suggests that the addition of graphite to PLA does not affect the biocompatibility of the material. This conclusion is in agreement with the literature that reports graphite as biodegradable [31] and biocompatible [32].

VI. PIEZORESISTIVITY CHARACTERIZATION – GRAPHITE-DOPED PLA

The gauge factor *GF*, i.e., the ratio between the normalized change in resistance R and the axial strain ε

$$GF = \frac{dR}{R}/\varepsilon \tag{1}$$

of the graphite-doped PLA was characterized by conducting uniaxial tensile tests on 3-D printed structures part of a Wheatstone bridge. The uniaxial tensile tests were carried out with a Pasco Materials Testing System ME-8230 (Pasco, Roseville, CA) at a uniform pulling rate of 4.76 mm/min and at a sampling rate of 25 Hz. The Wheatstone bridge was read at

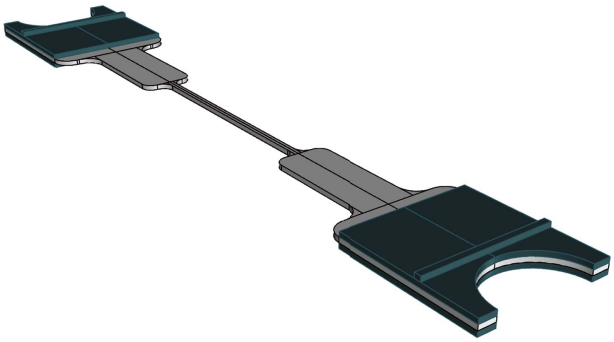

Fig. 13. Schematic (not to scale) of the test structure used to characterize the piezoresistivity of the graphite-doped PLA. The central beam is made of conductive PLA, while the top and bottom caps on both ends of the beam are made of dielectric PLA. The test structure has a ridge on both top caps to interface with the flat coupon fixture Pasco ME-8238.

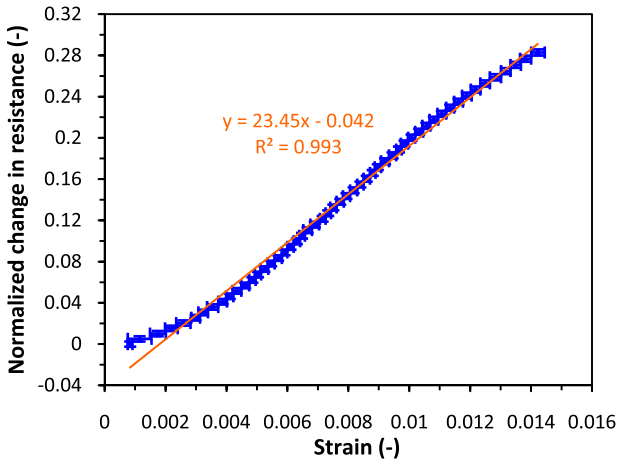

Fig. 14. Normalized change in resistance vs. strain of the graphite-doped PLA. A gauge factor of ∼23.5 is estimated from the data. Each data point is the average of 200 measurements.

a sampling rate of 25 Hz with a galvanometer Pasco PS-2160, while the bridge was energized with a Tekpower TP3005T variable linear DC power supply (Tekpower, Montclair, CA). The data were collected using the Pasco Capstone software –making sure that the data acquisition was synchronized.

Each 3-D printed test structure is a flat beam made of graphite-doped PLA that is sandwiched at the ends by caps made of dielectric PLA (Fig. 13); the caps electrically isolate the conductive beam from the ME-8230 and provide a clamping surface to the flat coupon fixture Pasco ME-8238. The conductive beam has a neck at its middle that is 0.6 mm thick, 0.8 mm wide, and 25 mm long, while the caps are 0.6 mm thick. The ends of the neck of the conductive beam were connected to the Wheatstone bridge using 160 μm diameter enameled copper wires and electrically conductive silver epoxy (MG Chemicals, Burlington, ON, Canada).

The curve of normalized change in resistance versus axial strain is shown in Fig. 14. The data are adequately described by a linear fit with a slope (gauge factor) equal to ∼23.5. Therefore, it should be feasible to create strain transducers based on piezoresistors, e.g., pressure sensors, made of extruded layers of dielectric and graphite-doped PLA. The *GF* of the FFF-printed graphite-doped PLA is an order of magnitude larger than that of metals (2-5) [33] and inkjet printed CNT strain sensors (∼3) [34], slightly smaller than the *GF* of carbon black-PDMS resistors (∼29) [35], and an order of magnitude smaller than the *GF* of single-crystal silicon (up to ∼200) [36].

VII. Examples of FFF-Printed, Biodegradable, Dielectric-Conductive Microsystems

A. Resistors, capacitors, inductors

Current research efforts in AM of electrical conductors for microsystems, particularly interconnects, focus on metal transfer and in-situ metal synthesis printing techniques. Printing methods based on transfer of metal nanoparticles include direct ink writing [9], electrohydrodynamic printing [37], and laser-assisted electrophoretic deposition [38], while printing methods based on transfer of metallic droplets include laser-induced forward transfer [39]. Printing methods based on in-situ synthesis of metals via chemical reduction include meniscus-confined electroplating [40], electroplating of locally dispensed ions in liquid form [41] and laser-induced photo-reduction [42], while printing methods based on in-situ synthesis via dissociation of metal precursors include focused electron/ion beam-induced deposition [43]. In many cases, the electrical conductivity of the imprints is very high –within an order of magnitude of the electrical conductivity of the bulk metal. However, these techniques have not been demonstrated as single-printing platforms that can also create dielectric structures to monolithically manufacture miniaturized dielectric-conductive devices.

Fifteen sets of resistor structures composed of conductive lines on top of a 1.2 mm thick dielectric plate were printed and characterized using a Fluke 287 multimeter with CAT II electrical probes. The structures were printed using 150 μm slices and 800 μm-wide conductive lines; in each set, the length of the resistors was varied between 6.4 and 65.6 mm and the height of the conductive lines was varied between 150 μm and 900 μm (Fig. 15(a)). The dimensions of the resistors were measured with a Nikon Microscope OPTIZOOM Module with a 0.8X-2.0X core zoom ratio, equipped with a Nikon M Plan 5X Objective and a 10X eyepiece. In most cases, the thickness of the printer resistors is a few microns larger than their nominal height. However, the 1-layer and 2-layer devices are ∼25 μm thicker (second column of Table VI); we speculate that the difference in thickness was due to homing/calibration issues during the printing of those samples. The printed resistors have a depression at their midline due to the interaction between adjacent stokes (Fig. 16); the depression was minimized by tuning the printing profile, e.g., the amount of overlapping between strokes, the printing speed, etc. (See section III.D).

The data grouped by the number of conductive layers are shown in Fig. 17. The data show a linear dependence between the length of the resistor and its resistance, as evidenced by the least square fitting. A contact resistance of about 200 Ω is present in the measurements. The electrical resistivity ρ was

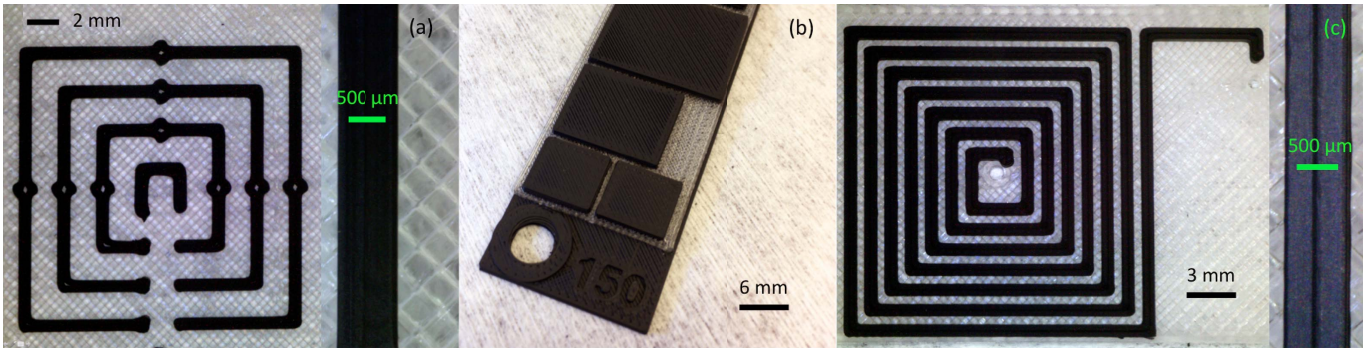

Fig. 15. (a) Top view of a set of printed resistors (left) and close-up of the conductive lines (right); (b) top view of a set of printed capacitors; (c) printed planar inductor (left) and detail of conductive line (right). The dielectric plate that supports the inductor includes printed holes for installing SMA connectors.

TABLE VI
ELECTRICAL RESISTIVITY AND SHEET RESISTANCE VERSUS THICKNESS OF CONDUCTIVE LAYER

Nominal thickness (µm)	Measured thickness (µm)	Resistivity (Ω.cm)	Sheet Resistance (Ω/□)
150	173.2	8.24	475.8
300	320.7	8.59	267.9
450	457.2	8.67	189.6
600	607.6	8.77	144.3
750	757.2	8.71	115.0
900	904.1	8.51	94.1

Each quoted measured thickness is an average of 150 measurements.

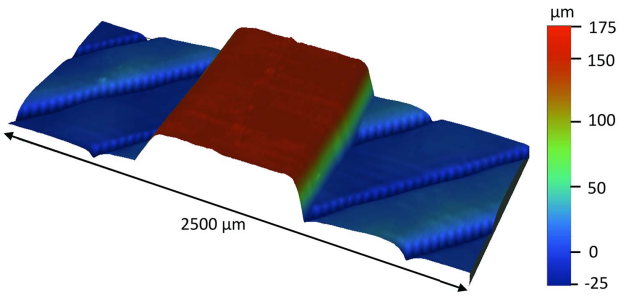

Fig. 16. Cross-section of a 1-layer resistor, evidencing a small notch at the midline due to the overlapping of adjacent nozzle strokes.

extracted from the linear fits as

$$\rho = \frac{dR}{dx} A_R \tag{2}$$

where R is the measured resistance, and x and A_R are the length and cross-section area of the resistor, respectively. The estimated average resistivity from all the data (Table VI) is $8.58 \pm 0.19\ \Omega \cdot$ cm –roughly the typical resistivity of a doped silicon wafer. The experimental results suggest that the interface between the layers does not cause significant changes in electrical resistance, probably because the layers are fused to the partially printed object as they are deposited. The electrical resistivity of the imprints made of conductive PLA is orders of magnitude larger than that of the imprints made with metal transfer and in-situ synthesis printing techniques, which could be as low as within an order of magnitude of the electrical resistivity of the bulk material [9], [37]–[43].

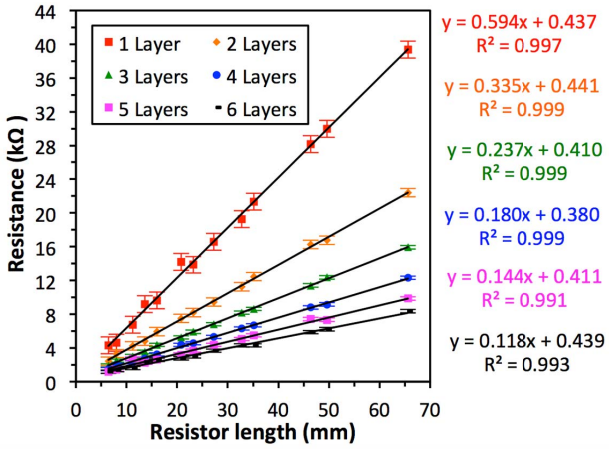

Fig. 17. Resistance vs. resistor length for conductive structures made with 150 μm layers. Each data point is the average of 15 measurements.

Therefore, the usefulness of the conductive PLA feedstock is limited in applications that involve large currents.

Fifteen sets of capacitive structures were printed using 150 μm layers. Each structure was composed of 12 capacitors that had as common electrode a 22 mm wide, 1.2 mm thick plate; the counter electrode was a 1.2 mm thick plate with area equal to 72, 180, or 380 mm^2 (Fig. 15(b)). The thickness of the dielectric layer between the electrodes was equal to 150, 300, or 450 μm. The capacitors were characterized at 10 kHz using a tweezers-style LCR meter LCR Pro1 (LCR Research, Toronto, Ontario, Canada) with 0.1% accuracy. In a parallel plate capacitor the capacitance C is

$$C = \varepsilon_r \varepsilon_o \frac{A_C}{\delta} \tag{3}$$

where ε_r is the relative electrical permittivity, ε_o is the electrical permittivity of free space, δ is the thickness of the dielectric, and A_C is the overlapping area of the capacitor plates. Fig. 18 shows the plot of $(C \cdot \delta/\varepsilon_o)$ vs. A_C; from the plot, a relative dielectric constant for the PLA dielectric layer equal to 2.61 is estimated; the result is in good agreement with the ~2.5 value for PLA from the literature for frequencies in the 100 Hz to 100 KHz range [44]. Based on the experimental results, the electrical relaxation time of the conductive PLA used in this study is equal to 2 ps; taking into account the HV

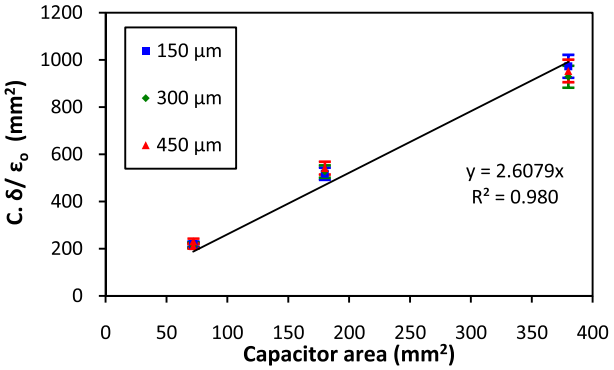

Fig. 18. Capacitance times dielectric thickness divided by electrical permittivity of free space versus electrode area. The data were obtained at 10 kHz. Each data point is the average of 15 measurements.

compatibility of the PLA feedstock (see section IV), it should be feasible to implement capacitive, miniaturized, MHz RF mass filters [46].

Planar square inductors were printed using 150 μm layers; the conductive lines were printed 1.5 mm tall to help reduce their electrical resistance (Fig. 15(c)). Measuring the inductance of these devices was unfeasible with our instrumentation because the resistance of the printed coil is in the ~10-25 kΩ range while the expected inductance is in the ~0.1-0.6 μH range [45], i.e., the reactance requires hundreds-of-MHz frequency signals to be comparable in magnitude to the resistance. This also evidences the impracticality of printing inductors with graphite-dope PLA or graphene-doped PLA; the manufacture of practical inductors likely requires significantly more conductive feedstock.

B. Cantilevers

Cantilevers are perhaps the most commonly used transducer in microsystems; examples include atomic force microscope (AFM) probes [47], energy harvesters [48], and biochemical sensors [49]. Several research groups have reported work on 3-D printed MEMS cantilevers. For example, Chan et al. demonstrated 2 mm wide, 450 μm thick, and 4 mm long hydrogel cantilevers printed with SLA [50]. Also, Credi et al. reported 600 μm wide, 200 μm tall, and 9 mm long magnetic cantilevers made with SLA [51]; their cantilevers were magnetic due to an electroless coating applied after printing, or due to mixing magnetite nanoparticles with the printable feedstock. In addition, Lam and Schmidt reported inkjet printed 50 to 100 μm wide, 2.8 μm tall, and 500 μm long cantilevers made of silver nanoparticles; after printing, the cantilevers were trimmed using a 248 nm laser. Moreover, Park et al. demonstrated MEMS mechanical switches based on 100 μm wide, 1.6 μm tall, and 500 μm long inkjet printed silver cantilevers [53]; as in the work of Lam and Schmidt, the cantilever gap is defined with a layer of support material that is eventually removed. To the best of our knowledge, there are no reports of monolithically FFF-printed, multi-material cantilevers.

Arrays of electrically isolated, conductive cantilevers were monolithically printed on top of a dielectric substrate (Fig. 19); these devices could be used as a switch if they interact

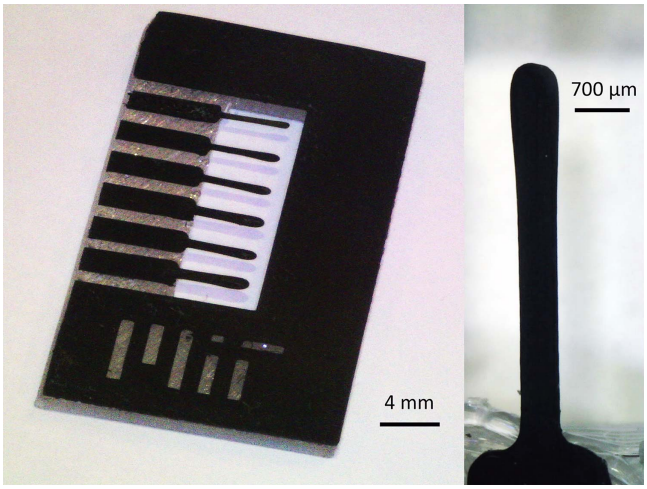

Fig. 19. A die with 6 cantilevers made of conductive PLA on top of a frame made of dielectric PLA; the cantilevers are 5 mm long, 500 μm to 900 μm wide, and 150 μm tall (left). Top view of a cantilever 5-mm long, 500 μm wide, and 150 μm tall (right).

with a conductive surface within their reach. The dielectric substrate is a rectangular frame 3 mm tall made of 7 mm wide beams that is intended to constrain the movement of the cantilevers at their roots. The cantilevers have rounded tips and roots with fillets because FFF prints continuous, closed loops of feedstock; the fillets and tip of a cantilever would be sharper if the nozzle diameter of the printer were smaller. The constrained end of each cantilever is connected to a 1.8 mm by 7 mm pad. The devices were 3-D printed upside-down, i.e., the top surfaces of the cantilevers were directly printed on top of the build plate, and the first layer of the dielectric frame was directly printed on top of the bottom of the cantilever pads; as explained in Section III.C, this is possible due to the bridging capability of the FFF technique. Two strategies were explored for releasing the devices from the build plate. In the first approach, the devices were detached by carefully pulling them using a M6 screw inserted into a mating threaded blind hole on the bottom of the dielectric frame (this is the procedure described in Section II to release the printed objects); given that the chips were printed upside-down, the threaded hole was readily accessible. Even though the devices could be successfully released using this procedure, sometimes the release procedure damaged the cantilevers. The second approach for releasing the cantilever chips entailed covering the build plate with a single layer of the water-soluble solder tape 3M 5414 [54] (3M, Electronics Materials Solutions Division 3M Center, St. Paul, MN) and printing the device directly on top of the tape. The tape has a 20 μm thick water-soluble adhesive layer in direct contact to the build plate, and a 33 μm thick PVA backing directly in contact with the printed part. After completing the printing job, the build plate is detached and rinsed with warm water –the tape is dissolved within 2 minutes leaving no residue, releasing the devices; finally, the chips are rinsed with warm water and gently dried with a nitrogen gun. There are no stitching issues in the application of the 3M 5414 tape to the build plate because the tape is wide enough to accommodate the footprint of the cantilever chip.

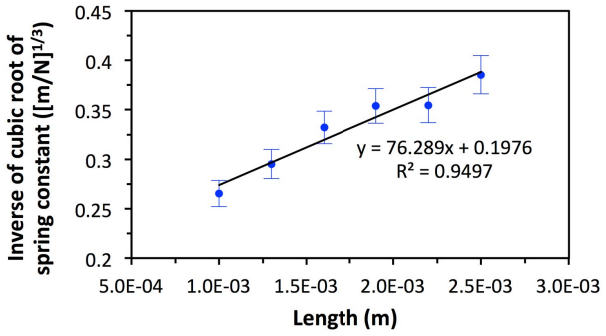

Fig. 20. Cubic root of the inverse of the spring constant versus distance from the root of the cantilever to the point of application of the force for a cantilever 500 μm wide and 150 μm tall made of conductive PLA. Each data point is the average of 15 measurements. The cross-section of the cantilever is a rectangle with 60 μm-radius rounded corners.

Characterization of the cantilevers was conducted with a Hysitron Triboindenter TI 950 (Hysitron, Eden Prairie, MN) using a 10-μm radius conic-spherical diamond tip; the instruments is capable of applying a force up to 10 mN with a resolution of 1 nN and noise floor of 100 nN, measuring vertical displacements up to 5 μm with a resolution of 0.04 nm and noise floor of 0.2 nm, and travelling a region of 300×150 mm in XY with a resolution of 500 nm. The spring constant k of a cantilever is the ratio of the applied force F to the vertical displacement w. In a cantilever made of an elastic, isotropic material with Young's modulus E and constant cross-section with area moment of inertia I, if the distance from the root to the point of application of the force is L, then k can be calculated as

$$k = F/w = 3E \cdot I/L^3. \tag{4}$$

The cross-section of the printed cantilevers is a rectangle of width W and height H with rounded corners of radius R_c; the moment of inertia of the cross section is

$$I = \frac{1}{12} W \cdot H^3 - R_c^4 \left(\frac{1}{3} - \frac{\pi}{4} + \frac{16}{9\pi} \right) - R_c^2 \left([H - R_c]^2 - \pi \left[\frac{H}{2} - R_c + \frac{4R_c}{3\pi} \right]^2 \right). \tag{5}$$

This model does not take into account the fillets at the root of the cantilever, which introduces error to its estimates. For a given geometry Eq. (4) predicts a linear relationship between the inverse of the cubic root of the spring constant and the point of application of the load; consequently, if the relative separation between the points of application of the load is well known, the estimate of the Young's modulus does not require to know the true length of the cantilever. We actuated the cantilevers far from the tip to avoid introducing error due to the rounded shape of the tip. From the force-deflection data a Young's modulus equal to 5.8 GPa is estimated for the conductive PLA (Fig. 20); analogous characterization of a 620 μm wide and 175 μm tall cantilever made of dielectric PLA yielded an estimated Young's modulus equal to 4.8 GPa, which is similar to the reported value by the manufacturer of the dielectric feedstock [55] and is lower than that of the conductive PLA. This is not surprising because the conductive PLA is dielectric PLA reinforced with graphite microparticles, and graphite can have a Young Modulus as high as 15 GPa [56].

C. Electrohydrodynamic liquid ionizers

Liquids can be ionized via electrohydrodynamic jetting, i.e., electrospray [57]. If electrospray emitters are miniaturized, they work with less voltage and consume less power; in addition, microfabrication makes possible to create monolithic arrays of miniaturized emitters with large array size and emitter density [58]. One of most important commercial applications of electrospray is ionization of liquid samples for mass spectrometry of biomarkers [59], which requires disposable electrospray sources to avoid cross-contamination. Our group recently demonstrated massively multiplexed SLA-printed MEMS electrospray sources [5] that are inexpensive enough to be disposable (each device uses ~$2 in printable resin and takes ~2h to make including post-printing cleaning and UV curing). In this paper, we present a novel 3-D printed multiplexed electrospray source with integrated extractor electrode and M6 microfluidic threaded port that is biodegradable, biocompatible, and an order of magnitude cheaper (Fig. 21). The inlet of the threaded port is connected to a two-level distributor that supplies liquid to a set of 7 hydraulic ballasts; the two-level design of the distributor helps uniformize the flow while accommodating for the dimensions of the threaded port and the footprint of the emitter array. The ceilings of the two levels of the distributor are supported by hexagonal arrays of 800 μm-wide, 1.2 mm-tall circular columns with 700 μm separation between adjacent columns. Each 24 mm-long hydraulic ballast has an internal diameter equal to 550 μm; the hydraulic ballasts are embedded into a panel structure that provides rigidity to the assembly while saving printable material. The hydraulic ballasts end in 7 emitters with 550 μm internal diameter and 725 μm wall thickness; each emitter spout is surrounded by a proximal extractor electrode 300 μm thick with 4.55 mm diameter aperture. The extractor grid is connected to the main body of the device by three posts; the posts make contact to the extractor far from the emitters to avoid an electric short in the event of beam interception. Each device takes about 45 min to make, is monolithically printed, there is no post-processing, and costs ~$0.30 in printable feedstock. Electrical characterization of a dry device yielded nA-level leakage current –over a 20-fold smaller than the smallest current measured in the wet experiments. Electrical characterization of the device in triode configuration using ethylene glycol (liquid feed grounded, extractor electrode biased at -4 kV, collector electrode 2 cm away from the extractor biased at -13 kV) yielded 100% beam transmission. Visual inspection of the active device suggested uniform operation. The per-emitter current vs. per-emitter flowrate characteristic has a power dependence with 0.6 coefficient (Fig. 22), which is close to the square-root dependence predicted by de la Mora's law for the cone-jet emission mode [60]. The 7-emitter FFF-printed devices have an emitter density of 5.5 emitters.cm^2; the same emitters could

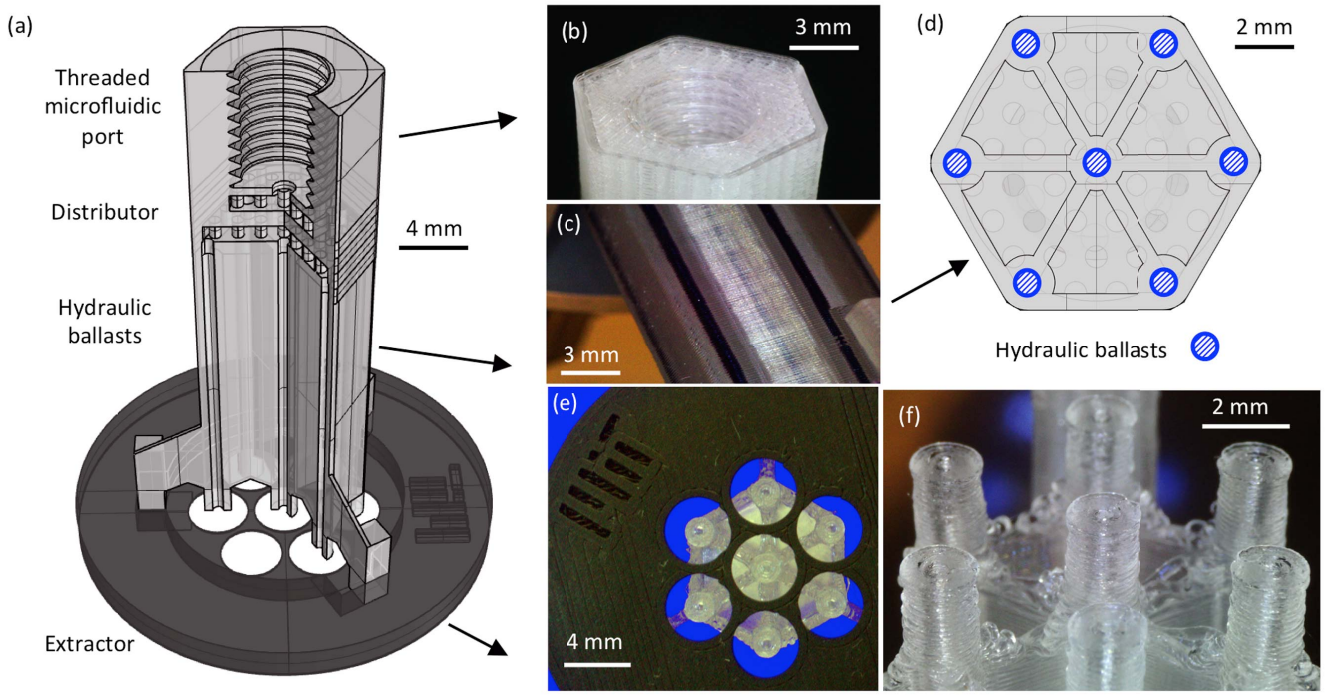

Fig. 21. (a) CAD schematic of FFF-printed 7-emitter electrospray array with hydraulics made of dielectric PLA and extractor electrode made of conductive PLA; (b) close-up of threaded microfluidic port; (c) close-up of hydraulic ballasts filled-in with red dye, evidencing 5 of the 7 hydraulic ballasts; (d) device cross-section showing the hydraulic ballasts embedded in the panel structure; (e) close-up of emitter head with integrated extractor electrode; (f) close-up of emitter spouts (for clarity, in this case the device was printed without extractor electrode).

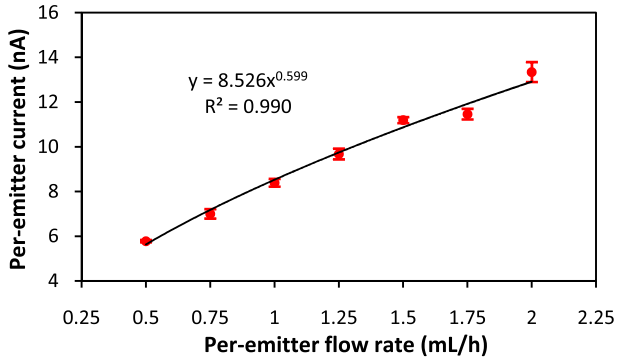

Fig. 22. Per-emitter current vs. flow rate characteristic for a fully-printed 7-emitter array with integrated extractor electrode and microfluidic port. Each data point in the plot is the average of 50 measurements.

be printed in densities as large as ~70 emittes.cm^2 if the requirement of no beam interception at the extractor is relaxed and adjacent emitters are allowed to share the wall. The array size of the FFF-printed device is a 33-fold smaller than the largest array we demonstrated with SLA printing in [5] (236-emitters, 236 emitters.cm^2). However, the 7-emitter array can be seen as a compromise between increasing electrical signal and device complexity (for a given flow rate, electrospray arrays operating in the cone-jet mode cause an increase in the total emitted current equal to the square root of the number of emitters [60]). Therefore, the 7-emitter array produces ~3 times more current than a single-emitter source fed the same flow rate, or ~6 times less current than the largest demonstrated SLA printed devices if fed the same flow rate.

VIII. Conclusion

This work explored the use of FFF printing to implement low-cost, monolithic, biodegradable, biocompatible, dielectric-conductive miniaturized systems using PLA as printable feedstock. Characterization of the feature resolution demonstrate close resemblance between CAD files and printed objects, with control of the vertical dimensions on the order of a few microns and control of the horizontal dimensions on the order of 25 μm. In addition, watertight microchannels with cross-section as small as 300 μm by 300 μm were demonstrated. Characterization of the surface topography of the printed parts found the amplitude of the horizontal and vertical waviness on the order of tens of microns, and roughness on the order of a few microns. Vacuum outgassing characterization of FFF-printed parts demonstrate compatibility with high vacuum applications and outgassing rates lower than those of commonly used polymers for vacuum. The viability of Jurkat immortalized human T-lymphocytes exposed to FFF-printed dielectric PLA and conductive PLA for 48 hours exhibited no statistically significant decline in cell viability relative to the positive control; furthermore, the cells exposed to the conductive PLA exhibited a response not statistically different from cells exposed to dielectric PLA, evidencing that the addition of graphite does not change the biocompatibility of PLA. Printed resistors and capacitors were demonstrated, as well as cantilevers and internally-fed electrohydrodynamic liquid atomizers.

With the graphite-doped conductive feedstock, applications that do not require transport of large currents can be satisfactorily implemented, e.g., low-current electrical

interfaces, electrostatic optics, electrospray ionizers, electrophoretic microfluidics [61], and MHz mass filters. In addition, the gauge factor of the graphite-doped conductive PLA was estimated at ∼23.5; therefore, it should be possible to print strain transducers based on piezoresistors, e.g., pressure sensors. Far more conductive PLA is commercially available, but requires direct drive extruders to be printed. With the more conductive feedstock, a wider range of applications could be satisfied, e.g., high-frequency devices, large-current electrical interfaces, and inductors. In particular, the demonstration of 3-D printed electromagnets would be of great interest, although it might require printing a third material for the core of the electromagnet coil to achieve a satisfactory performance.

ACKNOWLEDGMENT

The authors would like to thank Anthony Keen, Edwards Vacuum (Burgess Hill, UK), for conducting the outgassing experiments, Russell Singer, MAKEiT, Inc. (Alhambra, CA), for his valuable insights on FFF printing, Erika García, Massachusetts Institute of Technology (MIT, Cambridge, MA), for helping test the electrospray liquid ionizers, and Ashley Beckwidth, MIT, for helping test the cytotoxicity of FFF-printed dielectric PLA and conductive PLA samples.

REFERENCES

[1] M. Gad-el-Hak, Ed., *MEMS: Applications* (The MEMS handbook), 2nd ed. Boca Raton, FL, USA: CRC Press, 2006.

[2] S. D. Senturia, *Microsystem Design*, 1st ed. New York, NY, USA: Springer, 2004.

[3] M. Vaezi, H. Seitz, and S. Yang, "A review on 3D micro-additive manufacturing technologies," *Int. J. Adv. Manuf. Technol.*, vol. 67, nos. 5–8, pp. 1721–1754, Jul. 2013.

[4] A. K. Au, N. Bhattacharjee, L. F. Horowitz, T. C. Chang, and A. Folch, "3D-printed microfluidic automation," *Lab Chip*, vol. 15, pp. 1934–1941, Feb. 2015.

[5] L. F. Velásquez-García, "SLA 3-D printed arrays of miniaturized, internally fed, polymer electrospray emitters," *J. Microelectromech. Syst.*, vol. 24, no. 6, pp. 2117–2127, Dec. 2015.

[6] H. Gong, A. T. Woolley, and G. P. Nordin, "High density 3D printed microfluidic valves, pumps, and multiplexers," *Lab Chip*, vol. 16, pp. 2450–2458, May 2016.

[7] R. D. Sochol *et al.*, "3D printed microfluidic circuitry via multijet-based additive manufacturing," *Lab Chip*, vol. 16, pp. 668–678, Dec. 2016.

[8] D. Olvera-Trejo and L. F. Velásquez-García, "Additively manufactured MEMS multiplexed coaxial electrospray sources for high-throughput, uniform generation of core–shell microparticles," *Lab Chip*, vol. 16, no. 21, pp. 4121–4132, Oct. 2016.

[9] M. A. Skylar-Scott, S. Gunasekaran, and J. A. Lewis, "Laser-assisted direct ink writing of planar and 3D metal architectures," *Proc. Nat. Acad. Sci. USA*, vol. 113, no. 22, pp. 6137–6142, 2016.

[10] A. P. Taylor and L. F. Velásquez-García, "Miniaturized diaphragm vacuum pump by multi-material additive manufacturing," *J. Microelectromech. Syst.*, to be published, doi: 10.1109/JMEMS.2017.2743020.

[11] K. V. Wong and A. Hernandez, "A review of additive manufacturing," *ISRN Mech. Eng.*, vol. 2012, Jun. 2012, Art. no. 208760, doi: 10.5402/2012/208760.

[12] S.-Y. Wu, C. Yang, W. Hsu, and L. Lin, "3D-printed microelectronics for integrated circuitry and passive wireless sensors," *Microsyst. Nanoeng.*, vol. 1, Jul. 2015, Art. no. 15013.

[13] D. T. Pham and R. S. Gault, "A comparison of rapid prototyping technologies," *Int. J. Mach. Tools Manuf.*, vol. 38, nos. 10–11, pp. 1257–1287, 1998.

[14] *MP Select Mini 3D Printer V2, White*. Accessed: Sep. 6, 2017. [Online]. Available: https://Monoprice.com

[15] *Form 2 SLA 3D Printer—Formlabs*. Accessed: Sep. 6, 2017. [Online]. Available: https://formlabs.com/store/us/form-2/buy-printer/

[16] S. Waheed *et al.*, "3D printed microfluidic devices: Enablers and barriers," *Lab Chip*, vol. 16, no. 11, pp. 1993–2013, 2016.

[17] *Hyrel 3D Printers*. Accessed: Sep. 6, 2017. [Online]. Available: http://www.hyrel3d.com

[18] *ORD Solutions 3D Printers*. Accessed: Sep. 6, 2017. [Online]. Available: http://www.ordsolutions.com/3d-printers/

[19] *Polyjet Materials*. Accessed: Sep. 6, 2017. [Online]. Available: https://www.stratasysdirect.com/materials/polyjet/

[20] A. P. Gupta and V. Kumar, "New emerging trends in synthetic biodegradable polymers—Polylactide: A critique," *Eur. Polym. J.*, vol. 43, no. 10, pp. 4053–4074, 2007.

[21] F. Zhu, J. Skommer, T. Friedrich, J. Kaslin, and D. Wlodkowic, "3D printed polymers toxicity profiling: A caution for biodevice applications," *Proc. SPIE*, vol. 9668, p. 96680Z, Dec. 2015, doi: 10.1117/12.2202392.

[22] S. Abbott, "Chemical Compatibility of poly(lactic acid): A practical framework using hansen solubility parameters," in *Poly(Lactic Acid): Synthesis, Structures, Properties, Processing, and Applications*, S. Abbott, Ed. Hoboken, NJ, USA: Wiley, 2010.

[23] P. Azimi, T. Fazli, and B. Stephens, "Predicting concentrations of ultrafine particles and volatile organic compounds resulting from desktop 3D printer operation and the impact of potential control strategies," *J. Ind. Ecol.*, p. 13, Apr. 2017, doi:10.1111/jiec.12578.

[24] (1997). *Geometrical Product Specifications (GPS)—Surface Texture: Profile Method—Terms, Definitions and Surface Texture Parameters, ISO 4287*. Accessed: Sep. 6, 2017. [Online]. Available: https://www.iso.org/standard/10132.html

[25] (1996). *Geometrical Product Specifications (GPS)—Surface Texture: Profile Method—Rules and Procedures for the Assessment of Surface Texture, ISO 4288*. Accessed: Sep. 6, 2017. [Online]. Available: https://www.iso.org/standard/2096

[26] E. García-López, D. Olvera-Trejo, and L. F. Velásquez-García, "3-D printed multiplexed electrospinning sources for large-scale production of aligned nanofiber mats with small diameter spread," *Nanotechnology*, vol. 28, no. 42, pp. 425302-1–425302-12, Oct. 2017.

[27] *Bridging*. Accessed: Sep. 6, 2017. [Online]. Available: https://ultimaker.com/en/resources/19643-bridging

[28] K. Jousten, Ed., *Handbook of Vacuum Technology*, 2nd ed. Weinheim, Germany: Wiley-VCH, 2016.

[29] J. Blears, E. Greer, and J. Nightingale, *Advances in Vacuum Science and Technology*, vol. 2. Oxford, U.K.: Pergamon, 1960.

[30] R. J. Elsey, "Outgassing of vacuum materials-II," *Vacuum*, vol. 25, no. 8, pp. 347–361, 1975.

[31] P. A. Wagner, B. J. Little, K. R. Hart, and R. I. Ray, "Biodegradation of composite materials," *Int. Biodeterioration Biodegradation*, vol. 38, no. 2, pp. 125–132, 1996.

[32] P. I. Zolkin, "Study of graphite materials to be used in medicine," *Int. Polym. Sci. Technol.*, vol. 32, no. 9, pp. 67–68, 2005.

[33] A. L. Window, *Strain Gauge Technology*, 2nd ed. London, U.K.: Elsevier, 1992.

[34] Q. Li and Q.-M. Wang, "Inkjet printing of carbon nanotube-polyimide nanocomposite strain sensor," in *Proc. ASME Int. Mech. Eng. Congr. Expo.*, Phoenix, AZ, USA, 2016, p. 9.

[35] N. Lu, C. Lu, S. Yang, and J. Rogers, "Highly sensitive skin-mountable strain gauges based entirely on elastomers," *Adv. Funct. Mater.*, vol. 22, no. 19, pp. 4044–4050, 2012.

[36] S. Middlehoek and S. A. Audet, *Silicon Sensors*. Delft, The Netherlands: Delft Univ. Press, 1994.

[37] B. W. An *et al.*, "High-resolution printing of 3D structures using an electrohydrodynamic inkjet with multiple functional inks," *Adv Mater.*, vol. 27, no. 29, pp. 4322–4328, 2015.

[38] T. Takai, H. Nakao, and F. Iwata, "Three-dimensional microfabrication using local electrophoresis deposition and a laser trapping technique," *Opt. Exp.*, vol. 22, no. 23, pp. 28109–28117, 2014.

[39] M. Zenou, A. Sa'ar, and Z. Kotler, "Laser jetting of femto-liter metal droplets for high resolution 3D printed structures," *Sci. Rep.*, vol. 5, Nov. 2015, Art. no. 17265.

[40] J. Hu and M.-F. Yu, "Meniscus-confined three-dimensional electrodeposition for direct writing of wire bonds," *Science*, vol. 329, no. 5989, pp. 313–316, 2010.

[41] L. Hirt *et al.*, "Template-free 3d microprinting of metals using a force-controlled nanopipette for layer-by-layer electrodeposition," *Adv. Mater.*, vol. 28, no. 12, pp. 2311–2315, 2016.

[42] Y.-Y. Cao, N. Takeyasu, T. Tanaka, X.-M. Duan, and S. Kawata, "3D metallic nanostructure fabrication by surfactant-assisted multiphoton-induced reduction," *Small*, vol. 5, no. 10, pp. 1144–1148, 2009.
[43] V. Tasco *et al.*, "Three-dimensional nanohelices for chiral photonics," *Appl. Phys. A*, vol. 122, p. 280, Apr. 2016.
[44] K. Shinyama and S. Fujita, "Study on the electrical properties of a biodegradable plastic," in *Proc. 7th Int. Conf. Properties Appl. Dielect. Mater.*, Nagoya, Japan, 2003, pp. 707–710.
[45] S. S. Mohan, M. del Mar Hershenson, S. P. Boyd, and T. H. Lee, "Simple accurate expressions for planar spiral inductances," *IEEE J. Solid-State Circuits*, vol. 34, no. 10, pp. 1419–1424, Oct. 1999.
[46] M. Geear, R. R. A. Syms, S. Wright, and A. S. Holmes, "Monolithic MEMS quadrupole mass spectrometers by deep silicon etching," *J. Microelectromech. Syst.*, vol. 14, no. 5, pp. 1156–1166, Oct. 2005.
[47] S. R. Manalis *et al.*, "Interdigital cantilevers for atomic force microscopy," *Appl. Phys. Lett.*, vol. 69, no. 25, pp. 3944–3946, 1996.
[48] R. Elfrink *et al.*, "Vibration energy harvesting with aluminum nitride-based piezoelectric devices," *J. Micromech. Microeng.*, vol. 19, no. 9, p. 094005, 2009.
[49] N. V. Lavrik, M. J. Sepaniak, and P. G. Datskos, "Cantilever transducers as a platform for chemical and biological sensors," *Rev. Sci. Instrum.*, vol. 75, no. 7, pp. 2229–2253, Jul. 2004.
[50] V. Chan *et al.*, "Multi-material bio-fabrication of hydrogel cantilevers and actuators with stereolithography," *Lab Chip*, vol. 12, no. 1, pp. 88–98, 2012.
[51] C. Credi *et al.*, "3D printing of cantilever-type microstructures by stereolithography of ferromagnetic photopolymers," *ACS Appl. Mater. Interfaces*, vol. 8, no. 39, pp. 26332–26342, 2016.
[52] E. Lam and M. A. Schmidt, "Characterizing metal nanoparticle films: A methodology using surface micromachining by direct printing," in *Solid-State Sens., Actuators, Microsyst. Workshop Tech. Dig.*, Jun. 2012, pp. 433–436.
[53] E. S. Park, Y. P. Chen, T.-J. King Liu, and V. Subramanian, "Inkjet printed micro-electro-mechanical switches," in *Int. Electron Devices Meeting Tech. Dig.*, Washington, DC, USA, 2011, pp. 665–668.
[54] *3M Water-Soluble Wave Solder Tape 5414*. Accessed: Sep. 6, 2017. [Online]. Available: http://multimedia.3m.com/mws/media/147746O/3m-water-soluble-wave-solder-tape-5414-transparent.pdf
[55] *3D-Fuel's Advanced PLA*. Accessed: Sep. 6, 2017. [Online]. Available: http://www.3dfuel.com/advanced-pla/
[56] *Properties and Characteristics of Graphite*. Accessed: Sep. 6, 2017. [Online]. Available: http://poco.com/Portals/0/Literature/Semiconductor/IND-109441-0115.pdf
[57] G. Taylor, "Disintegration of water drops in an electric field," *Proc. R. Soc. Lond. A, Math. Phys. Sci.*, vol. 280, no. 1382, pp. 383–397, 1964.
[58] L. F. Velásquez-García, A. I. Akinwande, and M. Martínez-Sánchez, "A planar array of micro-fabricated electrospray emitters for thruster applications," *J. Microelectromech. Syst.*, vol. 15, no. 5, pp. 1272–1280, Oct. 2006.
[59] J. B. Fenn, M. Mann, C. K. Meng, S. F. Wong, and C. M. Whitehouse, "Electrospray ionization for mass spectrometry of large biomolecules," *Science*, vol. 246, no. 4926, pp. 64–71, 1989.
[60] J. F. de la Mora and I. G. Loscertales, "The current emitted by highly conducting Taylor cones," *J. Fluid Mech.*, vol. 260, pp. 155–184, Feb. 1994.
[61] R. K. Perdue *et al.*, "Bipolar electrode focusing: The effect of current and electric field on concentration enrichment," *Anal. Chem.*, vol. 81, no. 24, pp. 10149–10155, 2009.

Zhumei Sun received the B.E. degree (Hons.) in test control technique and instrument from the Beijing Institute of Technology, in 2013, and the M.E. degree in optical engineering from the Shanghai Institute of Optics and Fine Mechanics, Chinese Academy of Sciences, in 2016. She is currently pursuing the M.S. degree with the Department of Mechanical Engineering, Massachusetts Institute of Technology (MIT), and is part of the Velásquez-García's Group, MIT.

Before joining MIT, her previous research interests included the study of full-color dynamic computer-generated holographic 3-D displays and modal analysis of deep-etched subwavelength gratings. Her research interests include the 3-D printing of detail-rich, vacuum-compatible, and miniaturized systems.

Luis Fernando Velásquez-García (M'09–SM'10) received the mechanical engineer and civil engineer (*magna cum laude*) degrees (valedictorian of the School of Engineering in both cases) from the Universidad de Los Andes, Bogotá, Colombia, in 1998 and 1999, respectively, and the M.S. and Ph.D. degrees from the Massachusetts Institute of Technology (MIT), Cambridge, MA, USA, in 2001 and 2004, respectively.

In 2004, after completing his studies, he became a Post-Doctoral Associate with the Microsystems Technology Laboratories (MTL), MIT, where he was appointed as a Research Scientist in 2005. Since 2009, he has been a Principal Scientist and a Core Member with MTL. He is an Expert in micro and nanofabrication technologies. He leads a group that conducts research on micro and nano-enabled multiplexed scaled-down systems for space, energy, healthcare, manufacturing, and analytical applications that exploit high-electric field phenomena, e.g., electrospray, gas ionization, field emission, X-rays, and plasmas. He has authored over 40 journal publications and 60 conference proceedings publications. He holds 15 patents on MEMS/NEMS technologies. His research interests include additively manufactured micro and nanosystems. He served as the Co-Chair of the 15th International Conference on Micro and Nanotechnology for Power Generation and Energy Conversion Applications (PowerMEMS 2015).

Dr. Velásquez-García is a Full Member of Sigma Xi and a Senior Member of the American Institute of Aeronautics and Astronautics.